Biophysical Journal
Article

Biophysical Society

Quality control maps: Real-time quantitative control of single-molecule localization microscopy data

Sébastien Mailfert,[1] Meriem Djendli,[1] Roxane Fabre,[1] Didier Marguet,[1,*] and Nicolas Bertaux[2,*]
[1]Aix Marseille University, CNRS, INSERM, Centre d'Immunologie Marseille Luminy, Marseille, France and [2]Aix Marseille University, CNRS, Centrale Méditerranée, Institut Fresnel, Marseille, France

ABSTRACT Single-molecule localization microscopy (SMLM) has revolutionized the understanding of cellular organization by reconstructing informative images with quantifiable spatial distributions of molecules far beyond the optical diffraction limit. Much effort has been devoted to optimizing localization accuracy. One such approach is the assessment of SMLM data quality in real time rather than after lengthy postacquisition analysis, which nevertheless represents a computational challenge We overcame this difficulty by implementing an innovative mathematical approach we designed to drastically reduce the computational analysis of particle localization. Our quality control maps (QCM) workflow enables a much higher rate of data processing compared to that limited by the frequency required by current cameras. Accordingly, using an innovative computational approach for the detection step and an estimator based on a Gaussian model of the point spread function, subpixel particle locations and their accuracy can be determined through a straightforward analytical calculation without the need for iterations. As a true parameter-free algorithm, QCM is robust and adaptable to all types of SMLM data, with high speed enabling the real-time calculation of quantitative quality control indicators. Such features are compatible with smart microscopy, the concept of which depends on the adjustment of acquisition parameters in real time according to analytical results. Finally, the offline QCM mode can be used as a tool to evaluate synthetic or previously acquired data, as well as to teach the basic concepts of SMLM.

SIGNIFICANCE Although single-molecule localization microscopy (SMLM) is a powerful and informative imaging technique, it remains very time consuming, in terms of data acquisition, postprocessing analysis, and interpretation of results. All these steps require experimenters to hold a high level of expertise in order to generate reliable SMLM observations. To address these drawbacks, we developed quality control maps (QCM), the main features of which are 1) a graphical processing unit allowing fast analysis exceeding the performance of comparable algorithms, 2) real-time calculation of image quality indicators, and 3) a processing mode without parameter adjustment. Accordingly, QCM provides instant feedback from the launch and throughout the process of SMLM data acquisition, thus enabling experimenters to assess its accuracy and robustness.

INTRODUCTION

In systems biology, smart microscopy (SM) combined with powerful "omics" approaches can significantly bridge the gap between cellular events and organism-level phenomena and, ultimately, unravel complex biological networks (1). Combining cutting-edge hardware, sophisticated software, and powerful algorithms, SM facilitates the use of increasingly complex modalities required by photonic microscopy to provide key spatio-temporal observables (2). Indeed, SM-based automated data acquisition offers the possibility of easily and reproducibly combining imaging procedures in a single experiment. As the amount of information increases, real-time analysis-based or machine learning algorithm-based approaches enable on-the-fly adjustment of acquisition parameters (3) and/or the processing of large data sets to identify patterns, anomalies, and subtle changes, ultimately enabling autonomous decision-making or rapid and accurate diagnoses (4). Thus,

Submitted September 16, 2024, and accepted for publication February 21, 2025.

*Correspondence: marguet@ciml.univ-mrs.fr or nicolas.bertaux@centrale-marseille.fr

Sébastien Mailfert's present address is Aix Marseille Univ, CNRS, Centrale Méditerranée, Institut Fresnel, Marseille, France

Meriem Djendli's present address is Université Paris-Saclay, Institut des Sciences Moléculaires d'Orsay, CNRS, Orsay, France

Roxane Fabre's present address is Carl Zeiss SAS, Rueil-Malmaison, France

Editor: Gerhard Schütz.

https://doi.org/10.1016/j.bpj.2025.02.018

next-generation microscopes are poised to assist humans in automating the acquisition and analysis of data in regions of interest driven by specific events. To this end, providing real-time feedback is a prerequisite for adjusting parameters, optimizing imaging conditions, and dynamically exploring samples.

This requirement is particularly relevant to photonic microscopy approaches based on single-molecule localization microscopy (SMLM), which has revolutionized the understanding of cellular organization by reconstructing informative images on the nanoscale (5–8). SMLM observations can inherently produce high-resolution images from which biologically relevant information can be obtained, such as the nanostructure and stoichiometry of macromolecular complexes (9), provided that the SMLM data production process is properly mastered to resolve a given biological question (10,11). In this respect, many efforts have been made to optimize not only the sample preparation (unbiased fixation, labeling procedures, etc.) (12–16) but also the acquisition modalities (laser power, camera integration time, stabilized optical systems, etc.) (17–20) or the design of dedicated quantitative analytical methods (21–23).

The overall process of generating SMLM data, which includes image acquisition, handling, and analysis, is time consuming, and achieving localization accuracy while avoiding misleading interpretations is highly dependent on the quality of the data acquired. Thus, one computational challenge is estimating this localization accuracy before rather than after data acquisition in order to save time and avoid losing valuable samples (Fig. S1 *a*). However, most software packages, like NanoJ-SQUIRREL (24) or SuperStructure (25), ensure robust quantitative a posteriori analysis (see, for review, (26,27)) and, given that no further adjustment or correction of the acquisition parameters can be made, must assume the appropriate recording of data for super-resolution image reconstruction. For instance, NanoJ-SQUIRREL provides a quantitative assessment of SMLM results by generating a quantitative evaluation of super-resolution images to help experimenters optimize imaging parameters; this approach is based on comparing diffraction-limited images and super-resolution equivalents.

Analytical tools able to assess the quality and robustness of SMLM data at any time, thereby enabling a priori quantitative control of data, are, therefore, in high demand from a broad community of cell biologists (Fig. S1 *a*). The aim of any such tool is to carry out analyses in real time in order to adjust the acquisition parameters for optimal data recording. In a move away from the poor-quality and misleading data acquired through a posteriori analysis, such a real-time approach is expected to avoid time-consuming and unnecessary data acquisition. Some strategies have implemented new computational tools to speed up image acquisition or processing (28,29). Computer architecture design is another means of achieving high computing performance (24,28,30–34). One example is the graphics processing unit (GPU)-based software package QC-STORM (30), which, while able to perform real-time image processing and generate a list of particle localizations, lacks precise quantification, relies uniquely on full dataset indicators, and provides only histograms. Another method computes the Fourier ring correlation measurement in real time (35). Alternatively, hardware developments have been implemented to compute multi-emitter fitting in real time (32).

Considering the direct dependence of expected localization accuracy on two parameters—the signal/noise ratio (SNR) and the particle density per frame (D_{frame})—we designed and implemented quality control maps (QCM), a parameter-free algorithm that represents a major advance in the SMLM field and extends the single-particle tracking and SMLM algorithms previously developed (36,37). Classically, SMLM analysis consists of first detecting particles before estimating their positions, thus making it too slow to be compatible with a real-time evaluation of data quality. By implementing an original approach, we were able to harness the computing power of conventional computers to carry out the analysis of 2048 $\times$ 2048 pixel images at a rate of over 100 fps, thus making it suitable for real-time analysis. This involved rewriting the mathematical operations of the detection step, without impacting its robustness, using a generalized likelihood ratio test (GLRT) at a known background (37). For each pixel, three separable convolutions estimating the background, variance, and signal intensity, respectively, are processed, from which a detection map is generated. Then, thanks to a new estimator based on a conventional Gaussian model of the point spread function (PSF), it is possible to provide the subpixel particle localizations and their accuracy by simple literal calculation without the need for iterations.

Overall, the special feature of QCM is that it displays local (zoomed-in) and global (full-frame) quantitative maps and histograms in real time using a set of indicators that assess the quality of SMLM data in an easily understandable way thanks to color coding. These include the PSF size in *xy* and *xyz* positions, SNR, background, intensity, and localization accuracy. It should be noted that another major advance offered by QCM relies on the SNR (in dB) as the most relevant contrast parameter for summarizing expected achievable accuracy; indeed, the root mean-square of the localization accuracy, when expressed by SNR, depends weakly on noise model or density/frame (see the materials and methods section and Fig. S1 in (36)).

Thus, the workflow of the QCM software has been designed to conduct real-time data analysis, providing users with key observables in the decision-making process. If the results do not meet predetermined criteria, such as a

given molecular localization accuracy, then users can intervene in the setup, ensuring optimal acquisitions in line with the findable, accessible, interoperable, reusable (FAIR) data principles (38). Used prior to acquisition (Fig. S1 *b*, *left*), QCM primarily saves time, improves data relevance, and reduces data storage requirements. In addition, the use of QCM for postacquisition data analysis provides a standardized tool for educational purposes or for peer review of data (Fig. S1 *b*, *right*). To complement the online QCM mode, we have implemented a more versatile offline mode for use in evaluating and comparing datasets acquired previously or on different setups.

MATERIALS AND METHODS

UFUL

This section describes the mathematical basis of the ultrafast unsupervised localization (UFUL) concept. The acronyms and symbols used in the present study are consistent with those recapitulated in our previous study (see table S1 in the supporting material of (36)).

Computational optimization of the GLRT detection

The detection step is based on previous mathematical developments (36,37). In summary, when a particle is present, the PSF is modeled by a Gaussian $g_{p=\{i,j\}}(i_0,j_0,r_i,r_j)$ centered in $(i_0,j_0)\in\mathbb{R}^2$ and of dimensions r_i and r_j:

$$g_p(i_0,j_0,r_i,r_j) = \frac{1}{\sqrt{\pi r_i r_j}}\exp\left(-\frac{(i-i_0)^2}{2\,r_i^2}-\frac{(j-j_0)^2}{2\,r_j^2}\right), \tag{1}$$

where the normalizing constant is such that $\iint g^2 = 1$.

The detection theory cannot simultaneously estimate the value of the parameters (i_0,j_0,r_i,r_j) and the presence or absence of a particle (39). For the GLRT detector, the PSF is in the center of the window, and $r_i = r_j = r$ is known. Thus, the GLRT assesses the presence of a signal at each pixel such that $(i_0,j_0) = (i_n,j_n)|_{n\in\mathbb{N}}$. When a signal is detected, the estimator searches in (i_n,j_n) the subpixel positions (i_0,j_0) of the PSF. For a PSF in a window, it is easier to write $(i_n,j_n) = (0,0)$ for simplicity.

For a GLRT at a known background (36), the mean m and variance σ^2 of the background are known. This detector is based on the two H_0 and H_1 hypotheses, both perturbed by independent, identically distributed additive Gaussian noise. For H_0 in the working window ω, the signals at pixel $p = \{i,j\}$ are the sum of background m and noise n_p of variance σ^2:

$$H_0: x_p = m + n_p. \tag{2}$$

The H_1 hypothesis has a Gaussian centered in the window that is modeled by

$$H_1: x_p = \alpha\, g_p(0,0,r,r) + m + n_p, \tag{3}$$

where α is the particle intensity.

Let L_0 be the log likelihood of the H_0 hypothesis:

$$L_0 = -\frac{N}{2}\log\left(2\pi\sigma^2\right) - \frac{1}{2\sigma^2}\sum_{p\in\omega}\left(x_p - m\right)^2, \tag{4}$$

where N is the size of the window ω.

Let L_1 be the generalized log likelihood of the H_1 hypothesis:

$$L_1 = -\frac{N}{2}\log\left(2\pi\sigma^2\right) - \frac{1}{2\sigma^2}\sum_{p\in\omega}\left(x_p - \alpha\, g_p(0,0,r,r) - m\right)^2. \tag{5}$$

The estimated intensity is given by

$$\widehat{\alpha} = \frac{\sum_{p\in\omega} g_p\left(x_p - m\right)}{\sum_{p\in\omega} g_p^2}. \tag{6}$$

Thus, for a test based on the detection theory (39), the H_0 hypothesis is rejected with a probability of false alarm $(PFA)\in]0,1]$ if

$$2(L_1 - L_0) > \text{Inv}\,\chi^2(1-PFA,1), \tag{7}$$

with $\text{Inv}\,\chi^2(1-PFA,1)$ the inverse law of χ^2 with one degree of freedom. Thus, for a given *PFA*, this test discriminates a window containing noise alone from that containing a particle of SNR > 20 dB, with a detection probability $(PD)\approx 100\%$ (39).

The aim was to rewrite the GLRT expression to significantly optimize the computation time without compromising the robustness of the mathematical model.

Using $S_{PFA} = \text{Inv}\,\chi^2(1-PFA,1)$ as the detection threshold, the GLRT was rewritten for a given pixel as

$$2(L_1 - L_0) > S_{PFA}\ and \tag{8}$$

$$2\left[\left(-\frac{1}{2\sigma^2}\sum_{p\in\omega}\left(\overline{x} - \widehat{\alpha}\, g_p(0,0,r,r)\right)^2\right) - \left(-\frac{1}{2\sigma^2}\sum_{p\in\omega}(\overline{x})^2\right)\right] > S_{PFA}, \tag{9}$$

with $\overline{x} = x_p - m$.

Thus,

$$\frac{\widehat{\alpha}^2}{\sigma^2} > \frac{S_{PFA}}{\sum_{p\in\omega} g_p^2}. \tag{10}$$

This requires first estimating the background mean $\widehat{m}$ and variance $\widehat{\sigma}^2$ as previously described (see note S6 in the supporting material in (36)). In practice, they are estimated once every 50 frames.

This test can, therefore, be performed for all pixels of a given frame. Computing the left term of Eq. 10 simply as a convolution (Eq. 6) provides the corresponding image of the $\widehat{\alpha}$ and GLRT values of the pixels. When the test is true in the region of interest (ROI), it corresponds to a particle defined as a single pixel or as a set of pixels for bright ones, from which a list of detected particles with an integer pixel value is established.

Estimation of the particle localization

Once the particles are detected, the aim is to determine their subpixel localization, i.e., the subpixel position where $\widehat{\alpha}$ is maximum. Two computational methods are classically implemented.

1) Those based on an algorithm that performs oversampling of the $\widehat{\alpha}$ image and which are computationally expensive and unable to estimate the r_i, r_j radii of the PSF.
2) Those based on iterative fitting computation to estimate r_i, r_j, i_0, j_0 but which are time consuming.

The aim was to demonstrate that a third alternative is possible to determine the position of the particles and their radius with subpixel accuracy while guaranteeing an ultrafast computational speed, i.e., exceeding that of image acquisition.

The PSF is modeled by a Gaussian, and the algorithm uses the logarithm of $\widehat{\alpha}$ to obtain a quadratic expression. This enables a literal expression from which to derive the estimation of r_i, r_j, i_0, j_0, corresponding to the PSF sizes and subpixel coordinates of each particle, respectively.

As such, the current expression of $\widehat{\alpha}$ needs to be rewritten to provide a fast and efficient estimate of these r_i, r_j, i_0, j_0 parameters. By replacing m with its estimated value $\widehat{m}$, we obtain

$$\widehat{\alpha}_{\hat{m}} = \sum_{p \in \omega} \big(x_p - \widehat{m}\big) g_p(0,0,r,r). \tag{11}$$

However, $\widehat{\alpha}_{\hat{m}}$ does not correspond to the minimum mean-square error (MMSE) estimator that is expected from the solution given by $\widehat{\alpha}$. It is still possible to obtain a variance that coincides with that of the MMSE on the coordinates. When the H_1 hypothesis is true (Eq. 3), $\widehat{\alpha}_{\hat{m}}$ can be written as

$$\widehat{\alpha}_{\hat{m}} = \alpha \sum_{p \in \omega} g_p\big(i_0, j_0, r_i, r_j\big)\, g_p(0,0,r,r) + \sum_{p \in \omega} g_p\big(n_p + (m - \widehat{m})\big). \tag{12}$$

The second term, $\sum_{p \in \omega} g_p(n_p + (m - \widehat{m}))$, is noise processed by a matched filter, with the noise term on the estimate of m $(m - \widehat{m})$, implying that $\widehat{\alpha}_{\hat{m}}$ is a good approximation of an MMSE filter.

Ultrafast estimation of PSF dimensions and particle subpixel positions

We first establish the expression for estimating the intensity $\widehat{\alpha}_{\hat{m}}$ and the PSF sizes with logarithms. r_i, r_j represent the characteristic PSF sizes and i_0, j_0 the subpixel positions of the particle. Since PSF images modeled by Gaussians, filtered by a Gaussian kernel, generate Gaussians, the estimated intensity is therefore equal to

$$\widehat{\alpha}_{\hat{m}} = \alpha \sum_{p \in \omega} g_p\big(i_0, j_0, r_i, r_j\big)\, g_p(0,0,r,r) = \alpha\, k_q\big(i_0, j_0, r_i, r_j\big), \tag{13}$$

with $k_{q=(i,j)}(i_0, j_0, r_i, r_j) = \frac{2r\sqrt{r_i r_j}}{\sqrt{r_i^2+r^2}\sqrt{r_j^2+r^2}} \exp\left(-\frac{(i-i_0)^2}{2(r_i^2+r^2)}\right)\exp\left(-\frac{(j-j_0)^2}{2(r_j^2+r^2)}\right)$

The discrete second derivative on the i axis of the logarithm of $\widehat{\alpha}_{\hat{m}}$ calculated at the positions $(i_n, j_n) \in \mathbb{N}^2$ of the detected particles is

$$\log \widehat{\alpha}_{\hat{m}}(i_n + 1, j_n) - 2 \log \widehat{\alpha}_{\hat{m}}(i_n, j_n) + \log \widehat{\alpha}_{\hat{m}}(i_n - 1, j_n) = -\frac{1}{r_i^2 + r^2}. \tag{14}$$

The estimator of PSF sizes can be given as

$$\widehat{r}_i^2 = -\frac{1}{\log \widehat{\alpha}_{\hat{m}}(i_n + 1, j_n) - 2 \log \widehat{\alpha}_{\hat{m}}(i_n, j_n) + \log \widehat{\alpha}_{\hat{m}}(i_n - 1, j_n)} - r^2. \tag{15}$$

Considering the discrete first derivative on the i axis of the logarithm of $\widehat{\alpha}_{\hat{m}}$ as

$$\frac{1}{2}\left(\log \widehat{\alpha}_{\hat{m}}(i_n + 1, j_n) - \log \widehat{\alpha}_{\hat{m}}(i_n - 1, j_n)\right) = \frac{i_0 - i_n}{\widehat{r}_i^2 + r^2} \tag{16}$$

gives the estimator of i_0 as

$$\widehat{i}_0 = i_n + \frac{1}{2}\left(\log \widehat{\alpha}_{\hat{m}}(i_n + 1, j_n) - \log \widehat{\alpha}_{\hat{m}}(i_n - 1, j_n)\right)\left(\widehat{r}_i^2 + r^2\right). \tag{17}$$

Similarly, for the j axis, the estimators are

$$\widehat{r}_j^2 = -\frac{1}{\log \widehat{\alpha}_{\hat{m}}(i_n, j_n + 1) - 2 \log \widehat{\alpha}_{\hat{m}}(i_n, j_n) + \log \widehat{\alpha}_{\hat{m}}(i_n, j_n - 1)} - r^2 \tag{18}$$

and

$$\widehat{j}_0 = j_n + \frac{1}{2}\left(\log \widehat{\alpha}_{\hat{m}}(i_n, j_n + 1) - \log \widehat{\alpha}_{\hat{m}}(i_n, j_n - 1)\right)\left(\widehat{r}_j^2 + r^2\right). \tag{19}$$

Thus, by computing only five logarithms of the image $\widehat{\alpha}_{\dot{m}}$, i.e., $\log \widehat{\alpha}_{\dot{m}}(i_n, j_n)$, $\log \widehat{\alpha}_{\dot{m}}(i_n+1, j_n)$, $\log \widehat{\alpha}_{\dot{m}}(i_n-1, j_n)$, $\log \widehat{\alpha}_{\dot{m}}(i_n, j_n+1)$, and $\log \widehat{\alpha}_{\dot{m}}(i_n, j_n-1)$, all parameters $(\widehat{i}_0, \widehat{j}_0, \widehat{r}_i, \widehat{r}_j)$ for size and subpixel localization of any particle can be estimated.

Then, in addition to calculating $\widehat{\alpha}_{\dot{m}}(\widehat{i}_0, \widehat{j}_0, \widehat{r}_i, \widehat{r}_j)$ and the MSE to determine the SNR and variance of the error of the positions, it is necessary to calculate at the subpixel position, $\widehat{\alpha}_{\dot{m}}$, on these corresponding positions.

Evaluation of UFUL performance

All evaluations aimed at comparing the mathematical models or validating the algorithm were carried out on realistic synthetic data, i.e., those with levels of noise, signal, PSF size, particle density/frame, or image sizes typically encountered in SMLM experiments. The codes used to generate these datasets are available from the authors upon request.

For the comparison between UFUL and an MMSE estimator at different SNRs, signal-dependent noise is introduced as follows:

$$x_p = N\left(m_p, \sigma_p^2 = 2G\, m_p\right), \tag{20}$$

where G represents the gain of an electron multiplying charge-coupled devices (EMCCD) camera and is equal to one, and m_p represents the average of x_p and is defined as

$$m_p = \alpha\, g_p(i_0, j_0, r_0, r_0) + m.$$

The PSF SNR ranges from 20 to 40 dB, a PSF size $r_0 = 1.2$ pixels, and $m = 300$. 1000 noise draws were completed, each containing a particle randomly located in a one pixel square.

For the analyses of the UFUL performance as a function of PSF size, a synthetic dataset of 1000 noise draws, with an SNR set to 30 dB and, for UFUL, an adaptative filter size set to $r = 1.2$ pixels, was used with a working window of $\omega = 8 \times 8$ or 15×15.

For the analyses of the UFUL performance under conditions of three-dimensional (3D) astigmatism, particle localization is determined as a function of their optical axial position around z_0, the focal point. This was done on synthetic data mimicking image acquisition with an astigmatic lens (40). In this case, the PSF size (r_i, r_j) varies on the i and j axes in pixels from (1.2, 3.0) to (3.0, 1.2), and the dataset consists of 1000 noise draws, with an SNR set to 30 dB and, for UFUL, an adaptative filter size set to $r = 1.2$ pixels.

For the evaluation of the central processing unit (CPU)/GPU UFUL computation rate performance, the analyses were obtained as follows: on a DELL Precision 7740 laptop, CPU: E-2286M, 64 GB random-access memory (RAM), and GPU: NVIDIA Quadro RTX4000M. For CPU computations, the code was compiled in C for MATLAB (MEX) using Advanced Vector Extensions for 8-float 32-bit (single) operations to handle parallel computations. For GPU computations, the code was compiled with CUDA for MATLAB (MEX-CUDA). The computation times correspond to the analysis of 16-bit RAW images stored in the PC RAM, from which the detection/estimation process provides the list of particles (position, size of 2D or 3D PSF astigmatism, measured intensity, SNR, noise level, and position error) in the PC RAM.

QCM software package

A QCM package is freely available for academic and nonprofit users on the Recherche Data Gouv repository: https://doi.org/10.57745/85J9OU (see also the supporting material). It includes a user guide, a set of experimental and synthetic data, and the corresponding analyses. QCM is a multi-thread application developed in C/CUDA code on a LINUX platform (LINUX Ubuntu 20.04.2 LTS). It requires an NVIDIA GPU. Two modes are available (Figs. 1 *a* and S2).

1) The online mode requires a PCO (Edge 4.2 or 5.5 CLHS) sCMOS camera. The maximum frame acquisition rate is prioritized (i.e., ≈100 fps for 2048 × 2048 pixel images). QCM controls solely the camera of the imaging system. All other processes are run in parallel on specific and dedicated threads. This mode is fully adaptable to other types of

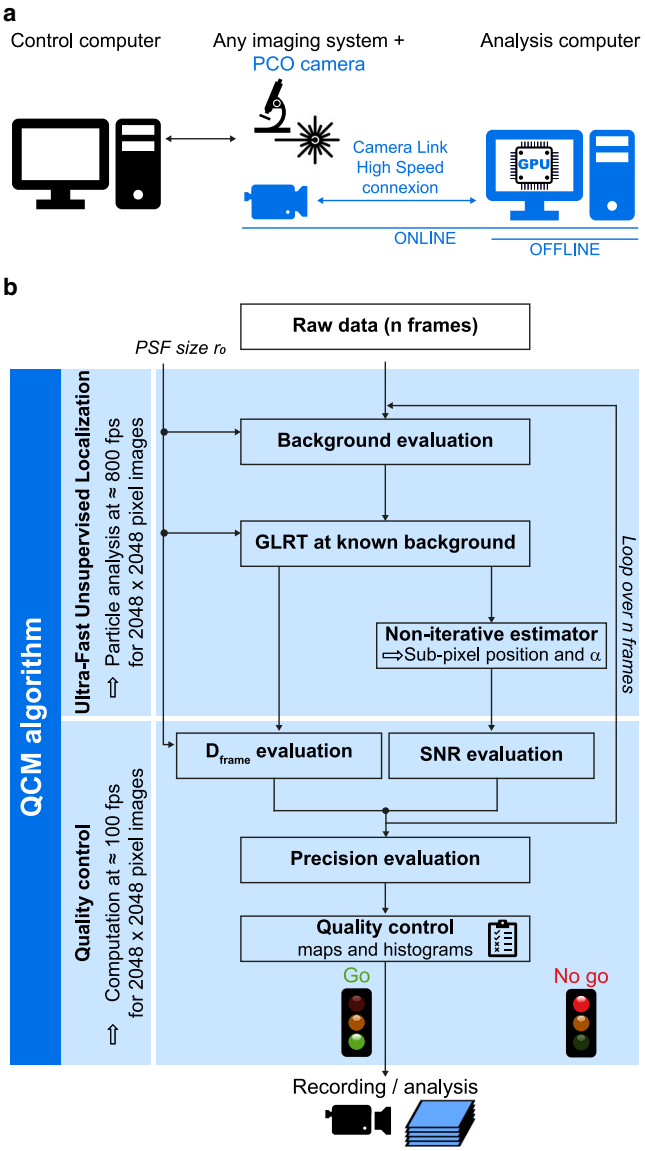

FIGURE 1 QCM modes and workflow. (*a*) The quality control maps (QCM) algorithm was originally designed to set optimal recording of single-molecule localization microscopy (SMLM) data operated on any imaging system equipped with PCO (Edge 4.2 CLHS or Edge 5.5 CLHS) sCMOS camera. It can be adapted to other cameras by utilizing and modifying the camera control and data acquisition functions through specific software development kits (SDKs). The offline mode can be used for the postacquisition evaluation of SMLM datasets. (*b*) The algorithm combines 1) the ultrafast unsupervised localization (UFUL) algorithm to perform the particle detection/localization steps at a rate of ≈800 fps for 2048 × 2048 pixel images, i.e., at a speed higher than that of image acquisition by current SMLM cameras, with 2) the quality control (QC) module for the real-time estimation of quality control indicators: density per frame (D_{frame}), signal/noise ratio (SNR), and localization accuracy (precision). The display of histogram distributions of these indicators in real time enables users to decide whether or not to start (online mode) or not (offline mode) analyzing an SMLM dataset. PSF, point spread function; GLRT, generalized likelihood ratio test; fps, frames per second.

camera, provided that two criteria are met: the availability of an appropriate software development kit on a Linux environment and a direct processing of large data transfers compatible with real-time analyses.
2) The offline mode has been developed for the postacquisition evaluation of datasets that are loaded from the hard disk and placed in the RAM of the processor. This mode is camera independent and thus only limited by the time required to load the SMLM dataset into the RAM.

Data acquisition and analysis

All acquisitions were made using total internal reflection fluorescence illumination on a custom-built system based on an inverted microscope (Nikon, Tokyo, Japan, TE2000-U) as previously described (36), with a CFI Apo TIRF 100× NA 1.49 oil immersion objective (Nikon), an argon/krypton multiline laser (Innova 70C-Spectrum, Coherent, Santa Clara, California), and an axial drift correction by the autofocus module, except for image acquisition, which was achieved with a PCO (Edge 4.2 CLHS) sCMOS camera (Excelitas Technologies, les Ulis, France) on a LINUX platform. The microscope was controlled with a homemade Labview v.2021 (National Instruments, Austin, Texas) code, and the data acquired using the QCM code.

Throughout the acquisition process, data are evaluated in real time with QCM to set the appropriate acquisition conditions. Postacquisition data analyses were performed with UNLOC (36) in high density mode with a high spatial frequency variation of background, a reconnection process with one off-state lifetime frame, and an integrated Gaussian rendering process after drift correction by correlation and without data filtering.

The raw experimental data illustrating the QCM performances are available from the authors upon request.

Reagents and sample preparations for experimental data

Quantitative experiments were performed starting with a calibration standard, i.e., DNA origami with GATTA-PAINT HiRes 80R nanorulers from GATTAquant, and the results were then evaluated using the corresponding GATTAnalysis v.1.5 software.

COS-7 cells (ATCC CRL 1651) and HeLa cells (ATCC CCL-2) were grown in DMEM (Gibco, Waltham, Massachusetts) supplemented with 10% fetal bovine serum, 10 mM HEPES, 2 mM L-glutamine, 1 mM sodium pyruvate (Gibco), and 1% penicillin/streptomycin (Gibco).

For the dSTORM experiments, cells were plated on coverslips N° 1.5 of 18 mm diameter (Marienfeld, Lauda-Königshofen, Germany, #0117580) and incubated at 37°C and 10% CO_2 for 48 h before beginning staining procedures. Cells were washed twice with prewarmed (37°C) phosphate-buffered saline (PBS) before being fixed with 4% paraformaldehyde in PBS for 15 min at room temperature, washed with PBS and treated with 50 mM $NaBH_4$ for 10 min to reduce background fluorescence, and finally washed with PBS. Fixed cells were permeabilized with 0.3% TritonX-100 in PBS for 30 min before being washed three times in PBS and then saturated with 3% bovine serum albumin (BSA) in PBS for 45 min to reduce unspecific labeling. Nuclear pore complex protein Nup133 or β-tubulin were labeled overnight at 4°C with rabbit anti-Nup133 antibody (Abcam, Cambridge, United Kingdom, #ab155990) and mouse anti-human β-tubulin monoclonal antibody (mAb; Sigma-Aldrich, St. Louis, Missouri, #05-661-I), respectively. Cells were then washed five times with 1% BSA in PBS before being incubated for 30 min at room temperature with Alexa Fluor 647 AffiniPure goat anti-rabbit immunoglobulin G (H+L) (Jackson ImmunoResearch Europe, Ely, United Kingdom, #111-605-003) for Nup133 labeling and Alexa Fluor 647-conjugated F(ab')2-goat anti-mouse immunoglobulin G (H+L) (Thermo Fisher Scientific, #A-21237) for β-tubulin. After five washes with 1% BSA in PBS, cells were fixed again with 2% paraformaldehyde in PBS for 5 min. Finally, after three washes in PBS, samples were mounted onto a depression slide with freshly prepared dSTORM buffer (50 mM Tris and 50 mM NaCl [pH 8.0] and supplemented with 50 mM cysteamine). Samples were then sealed with Twinsil Speed 22 (Picodent, #1300 1002) ready for imaging.

For the two-color DNA-PAINT experiments, the HelaCells_Tubulin_Tom20 smart samples (Abbelight, Cachan, France) were prepared in μ-slide VI 0.5 (IBIDI, Fitchburg, Wisconsin, #80607) using the microfluidic system Smart Flow (Abbelight) and the Smart Staining Kit following the manufacturer's instructions (Abbelight). The DNA-PAINT kit was then used following the manufacturer's instructions (Massive Photonics, Munich, Germany, #MASSIVE-sdAB-FAST 1-PLEX), applying anti-mouse and anti-rabbit nanobodies to recognize the mouse anti-α-tubulin mAbs (Sigma-Aldrich, #T6188) and rabbit recombinant anti-TOM20 mAbs (Abcam, #ab232589), respectively. The α-tubulin and mitochondria were detected in a unique imaging buffer with a mix of imager 1 (Cy3b) at a final concentration of 0.5 nM, and imager 2 (ATTO 655) at the specified concentration, respectively. Sequential acquisition was performed with a stack of 50,000 frames recorded at 514 nm (200 mW) using a 525/50 filter for α-tubulin, and a stack of 20,000 images was recorded at 647 nm (155 mW) using a 710/75 filter for TOM20.

RESULTS

The QCM heuristic

The QCM algorithm is divided into two main modules: UFUL and quality control (QC) (Fig. 1 *b*). The first is based on an innovative mathematical approach designed to drastically reduce the number of computational steps involved in particle localization analysis. As a result, UFUL performs the particle detection/localization steps at a much faster rate compared to frame rate acquisition by standard cameras used in SMLM. The second module then uses the UFUL results to estimate the relevant SMLM indicators in real time and displays their histogram distributions and map representations.

Classically, single-particle localization involves a detection step followed by an estimation at high resolution (i.e., subpixel) of the particle position in the (i, j) plane along with the size of the PSF on the i and j axes (37). To solve this problem, the regular procedure is based on a maximum likelihood estimator or an MMSE estimator. The main objective is to avoid using estimators on an ROI devoid of particles.

Within this field, we have previously provided mathematical developments to optimize the detection step by implementing a GLRT at a known background (36), i.e., for which we know the mean m and variance σ^2. This test is an effective unsupervised detection tool, the threshold of which is set by the *PFA* (41–43); it is primarily designed as a detector in an ROI with a working window of dimension ω for the absence (H_0 hypothesis) or presence (H_1 hypothesis) of a particle. The GLRT can also be conceived as an estimator since, under the H_1 hypothesis assumption, it builds the intensity image using an estimator similar to the MMSE estimator, which is close to the Cramér-Rao bound (CRB). As such, the GLRT performs an adaptive filtration in order to estimate the intensity, as previously described

(see, for instance, supplementary note 2 in (36)). However, its application as initially conceived cannot handle the real-time data flow of SMLM acquisitions.

To overcome this difficulty, we have rewritten the mathematical operations of the GLRT detector at a known background to considerably accelerate the computational steps without impacting the robustness of the test (see materials and methods for details). Practically, this implies firstly evaluating the mean $\widehat{m}$ and variance $\widehat{\sigma}^2$ of the background as in (36). The GLRT then assesses the presence of a signal at each pixel, and when a signal is detected, the estimator searches the subpixel positions of the PSF. UFUL computes $\widehat{\alpha}_{\widehat{m}}$ as the expression of the intensity $\widehat{\alpha}$ minus the image background $\widehat{m}$. Three separable convolutions are processed for each pixel to estimate the background, its variance, and the signal intensity $\widehat{\alpha}$, respectively. It is then possible to estimate the subpixel position of each detected particle and the size of its PSF. To do this, the PSF is modeled by a Gaussian function from which UFUL uses a logarithm of the intensity $\widehat{\alpha}$ to derive literal expressions for estimating PSF radii r_i, r_j and subpixel coordinates i_0, j_0 on axes i and j, respectively, for each particle.

It should be noted that UFUL has been designed to maintain the best performance, as shown by the evaluation results being all close to the CRB. It involves simply calculating straightforward, noniterative expressions based on a Gaussian PSF model. More complex PSF models cannot be ruled out but would imply the development of an estimator that would considerably slow down the computation rate and, consequently, compromise the possibility of assessing the quality of SMLM data in real time and adjusting their conditions of acquisition accordingly.

Evaluation of UFUL performance

To test the UFUL performance to ascertain whether analyses coincided with MMSE estimation with respect to the variances in positions, we used synthetic data with realistic levels of noise, signal, PSF size, etc., such as typically observed in experimental SMLM.

We first tested the accuracy of determining particle position as well as the probability of detection at different SNR levels ranging from 20 to 40 dB (Fig. 2). The performance of UFUL was very similar to that of an MMSE estimator, with both being close to the CRB. For a *PFA* of 10^{-6}, PD $\approx$ 100% for any SNR > 20 dB.

We next compared UFUL to an MMSE estimator as a function of differences in the PSF size ranging from $r = 1.0$ to 2.0. When the GLRT detector was made with a small working window $\omega = 8 \times 8$ (Fig. S3 *a*), while MMSE results were biased, UFUL allowed a good estimation of i_0, j_0, r_0 with a slight bias on $r > 1.6$ yet a variance $\sigma_{\widehat{r}}$ slightly above the CRB. For UFUL, the variance in particle positions is comparable to that of MMSE and close to the CRB, where accuracy of the adapted filter of UFUL on the synthetic data

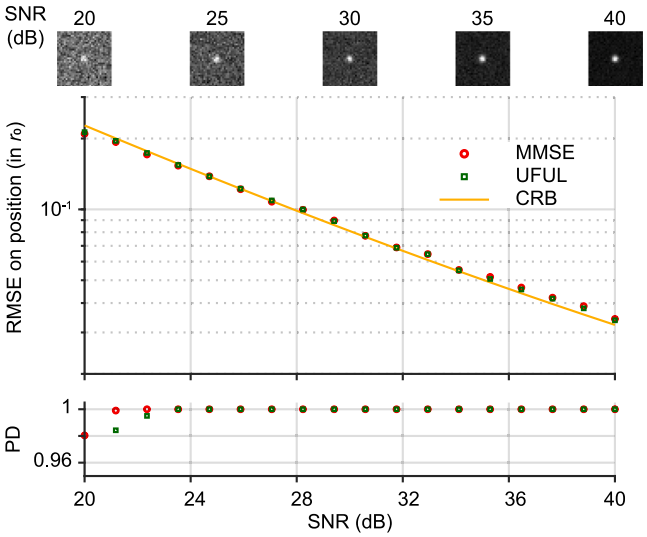

FIGURE 2 Performance of the UFUL estimator as a function of the SNR. The UFUL performance was compared to a minimum mean-square error (MMSE) estimator on a synthetic dataset of 1000 noise draws, with different SNRs ranging from 20 to 40 dB and, for UFUL, an adaptive filter size set to $r = 1.2$ pixels. The root mean-square error (RMSE) on the determination of particle position, expressed in r_0, and the probability of detection (PD) of the GLRT are both plotted as a function of SNR, expressed in dB. Thumbnails illustrate, at a given SNR, one of 1000 simulated images performed with PSF size $r_0 = 1.2$ pixels and background mean $m = 300$. CRB, Cramér-Rao bound.

depends on $r = r_0 = 1.2$. Similar analyses for a working window of $\omega = 15 \times 15$ (Fig. S3 *b*) led to little bias in the MMSE estimator results and a variance of $\widehat{r}$ very close to the CRB. Overall, UFUL provides, with an accuracy close to the CRB, the estimation of r on both i and j axes with the estimator $\widehat{r} = (\widehat{r}_i + \widehat{r}_j)/2$ regardless of PSF and working window size.

Satisfied that UFUL enables the estimation of PSF on both i and j axes, we then tested its performance determining the localization of particles as a function of their optical axial position around z_0, the focal point. We generated a synthetic dataset mimicking image acquisition with an astigmatic lens (40), in which the axial PSF of a particle is distorted in the i and j axes of the focal plane as a function of the particle's position on the optical axis, enabling it to be localized in 3D (Fig. S4). Under these conditions, the size of the working window ω for the GLRT detector set at 8×8, 10×10, 12×12, 14×14, or 16×16 pixels depends on r_0, the size of the PSF. As a result, the PSF sizes are well estimated with a slight bias of around 3.0 pixels (Fig. S4). To be fully integrated within the QCM software, this feature would require the development of another estimator but at the cost of slowing down the calculation rate and compromising real-time analyses.

Of note, UFUL, tested on a wide range of systems equipped with EMCCD or sCMOS cameras, has demonstrated good levels of performance analyzing SMLM data, irrespective of the electronics, pixel size, amplification mode, or noise characteristics of these cameras.

UFUL computation rate performance

We evaluated the UFUL performance on synthetic datasets generated at a given density of particles per frame and for different image sizes (Fig. 3). The analyses were obtained on a computer with the option of processing data with a CPU or GPU (see materials and methods for the specifications).

The performance levels are expressed in number of frames analyzed per second (Fig. 3 *a*). The computation times correspond to the analysis of 16-bit raw images stored in the PC RAM, from which the detection/estimation process returns a list of particles with position, size of 2D or 3D PSF astigmatism, intensity, SNR, noise level, and position errors in the PC RAM. Time mainly results from that used by the GLRT detector and at D_{frame} values ranging from 0 to 0.2 part/μm^2/frame; the number of particles has hardly any impact on the performance of detection/estimation steps (Fig. 3 *a*).

The UFUL module incorporates a computing segment specifically designed to optimize computation time to achieve a data flow of over 5 GB/s, enabling it to perform data analysis at a rate well above the acquisition performance of a standard SMLM camera, i.e., $\approx$100 fps for 2048 $\times$ 2048 pixel images. Indeed, with the GPU, the analysis rate for particle detection and position estimation reaches over 10,000 fps for 256 $\times$ 256 pixel images and up to $\approx$800 fps for 2048 $\times$ 2048 pixel images (Fig. 3 *a*). Furthermore, GPU computing increases the number of particles analyzed per second by up to 10-fold compared to CPU computing on large images (Fig. 3 *b*). For the GPU, images of sizes equal to or greater than 512 $\times$ 512 pixels present a similar number of particles analyzed per second, unlike the CPU, where the cache miss is significant.

Overall, the GPU speeds up analysis considerably when compared to the CPU, with a more noticeable difference on large images. It should be noted, however, that while the UFUL computation rate with a GPU is well above the frame rate of an SMLM camera, performance with a CPU remains above this threshold for images up to 1024 $\times$ 1024 pixels (Fig. 3 *a*). As a result, the second module of QCM can process the output of UFUL results and display the relevant QC indicators in real time.

QC module and the QCM interface

The QC module relies on UFUL results for the image background, particle positions, intensity, and PSF size. It evaluates in real time the key QC indicators—D_{frame}, SNR, and precision of localization parameters—and displays them using histograms and maps. We set up a graphical interface to facilitate the interpretation of the results from the real-time evaluation of QCM analyses (Fig. 4; Video S1). In the opening panel, QCM requires no parameterization other than the following physical parameters (Fig. S5).

1) The characteristic PSF radius (r_0) of the optical system, a physical characteristic inherent in the optical system for a given excitation wavelength and numerical aperture of the objective. This value must be expressed in pixels. As part of internal QC, QCM displays the r_0 histogram evaluated during data acquisition. Note that in the offline mode, r_0 can be set to "auto," and then QCM becomes completely parameter free.
2) The binning and exposure times of the camera.

QCM displays the histograms of PSF radius (r_0), D_{frame}, SNR, and precision parameters in real time. Analyses are visualized on the last 50, 500, or full stack of images; it is

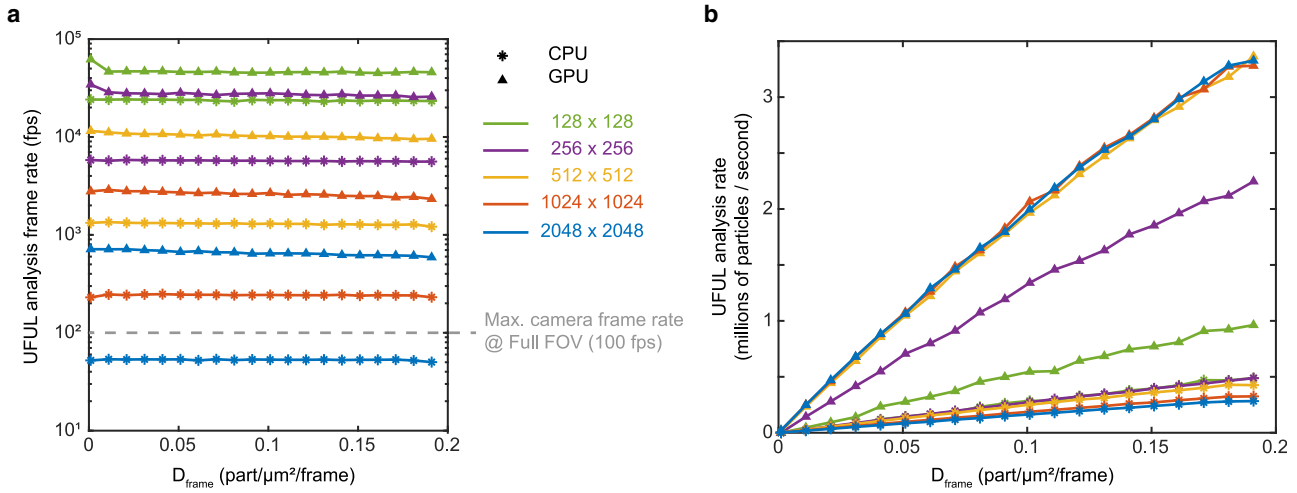

FIGURE 3 Comparison of central processing unit (CPU) and graphics processing unit (GPU) UFUL computation rates as a function of D_{frame} and image size. (*a*) Number of frames analyzed per second (fps) based on given D_{frame} values for images ranging from 128 $\times$ 128 to 2048 $\times$ 2048 pixels. (*b*) UFUL analysis rate expressed as number of particles detected and estimated position per second as a function of D_{frame} for different image sizes.

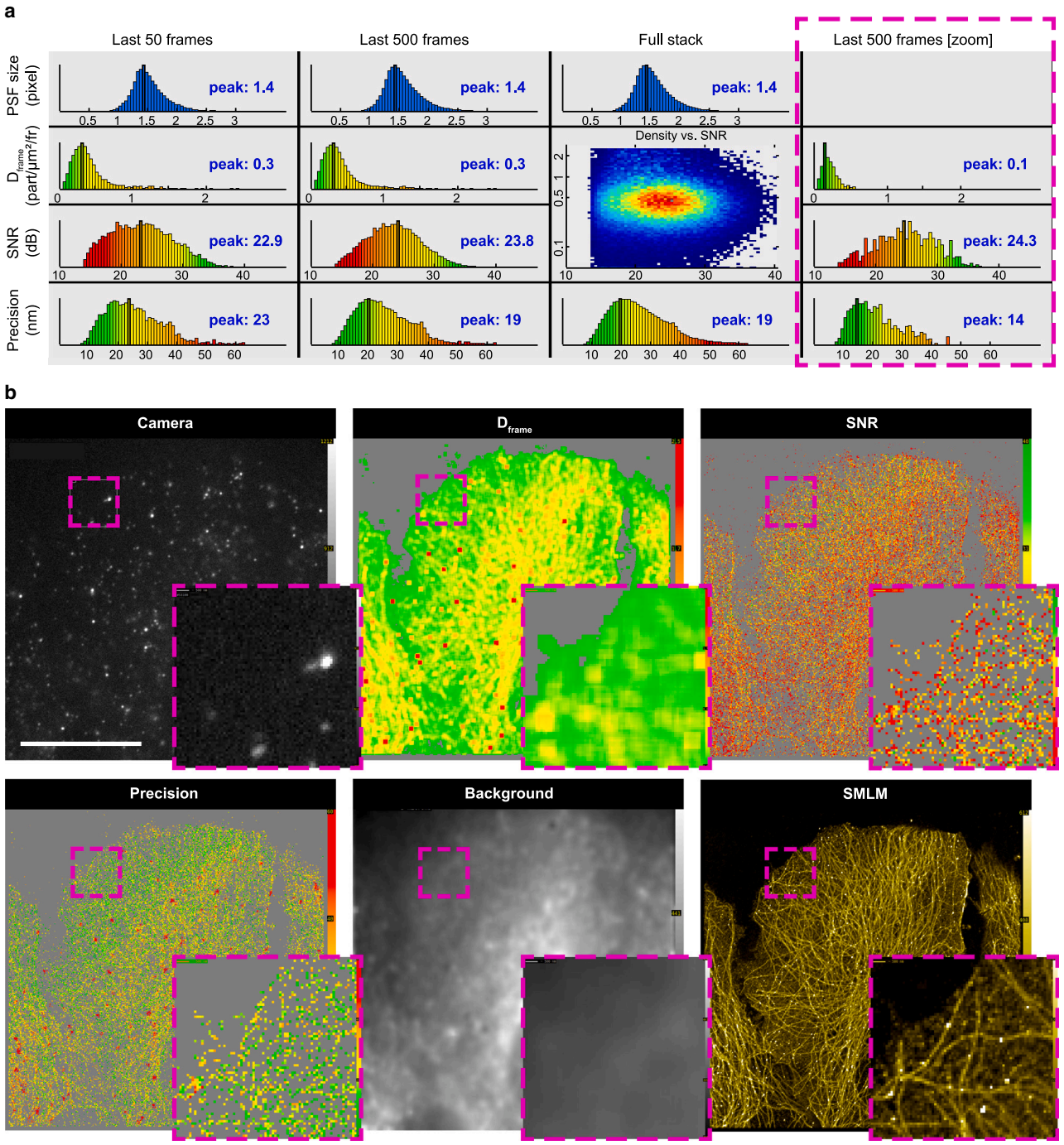

FIGURE 4 QCM quantitative indicators. (*a*) Real-time histograms of the PSF size r_0 (pixels), D_{frame} (particles/μm^2/frame), SNR (dB), and precision (localization accuracy; nm) can be displayed for the last 50, 500, or cumulative full field of view (FoV) frames or the last 500 frames on a zoomed region of interest (ROI) as illustrated with dSTORM imaging of β-tubulin in COS-7 cells. (*b*) Real-time QCM windows. Camera: live full FoV or zoomed area recorded by the camera; D_{frame}: color-coded D_{frame} values; SNR: color-coded SNR values; precision: color-coded root mean-square of localization accuracy estimated by combining D_{frame} and SNR indicators; background: background intensity; SMLM image: compilation of detected particle localizations. Scale bar: 20 μm for FoV and 10 μm for zoomed ROI.

also relevant for specific applications to estimate these indicators on a zoomed ROI (Fig. 4 *a*; Video S2). Moreover, when addressing a certain biological question requires a given accuracy for SMLM (e.g., dimensionality or count of macromolecular complexes, inter-distances between macromolecular structures, etc.), QCM offers the option of displaying the density-SNR space diagram in real time, thereby allowing the standardized evaluation of

experimental data. Other options enable the display of images captured by the camera, the reconstructed SMLM image, or those depicting QC indicators (background, D_{frame}, SNR, and precision parameters) (Fig. 4 *b*). Moreover, to ensure an accurate estimation of these parameters, QCM only displays the histograms when a minimum number of frames have been analyzed. This introduces an acceptable short latency of less than 1 s for the acquisition of 2048 × 2048 pixel images.

Finally, we would like to point out that the detection/estimation achieved by UFUL is primarily designed for image analysis under low-density conditions, i.e., D_{frame} less than ≈ 0.2 particles/μm^2/frame. To overcome this limitation, a density evaluation calibration has been integrated to ensure the algorithm returns realistic density values (see Note S1). The analysis obtained with QCM gives a very good estimate of the raw data that, nevertheless, then requires final analysis with a dedicated algorithm based on heuristics for reliable particle localization at variable local densities, such as UNLOC (36).

Assessment of QCM analyses robustness with nanoruler calibration standards

To assess the robustness of QC indicators calculated by QCM, we collected stacks of 2000 images of DNA origami nanorulers as nanoscopic benchmark structures (44). The SMLM DNA-PAINT imaging technique is used to assess the metrological traceability of nanorulers with mark-to-mark distances of 80 nm. The data acquired at different laser powers and camera integration times were analyzed in real time by QCM. Each initial acquisition is short, around 1 min per condition, but long enough to display informative SNR and D_{frame} histograms used to decide whether or not to continue data acquisition. QCM results were compared with those obtained on the same dataset using UNLOC and GATTAnalysis as postacquisition analysis tools (Fig. S6). As illustrated, the images reconstructed by UNLOC provide a qualitative estimate of the nanorulers, while GATTAnalysis evaluation is based on three parameters: the pass ratio, i.e., the percentage of good spots; the mark-to-mark distance in nm; and the fraction of nanorulers exceeding the accuracy threshold by 20 nm. For example, D_{frame} and SNR histograms provided by QCM peak at 1.3 particles/μm^2/frame and 22.4 dB, respectively, with conditions of acquisition set at 37 mW laser power and 36 ms camera integration time. Under such conditions, we cannot expect to ensure robust SMLM resolution, as assessed by postacquisition analyses, where only 12% of nanorulers achieve accuracy better than 20 nm. A go/no-go decision based on the SNR and D_{frame} histogram distribution provided by QCM analyses on a small number of frames is in good agreement with the results of postacquisition analyses provided by the UNLOC or GATTAnalysis algorithms. Therefore, QCM enables instant adjustment of camera integration time and/or laser power toward the optimal acquisition parameters necessary to achieve the highest possible localization accuracy on the samples before the initiation of SMLM data acquisition.

QCM-optimized SMLM acquisition on biological samples

To investigate the robustness of the key parameters SNR and D_{frame} histograms, we compared the QCM results obtained on the first stack of 2000 images of a biological sample before initiating data recording with those obtained by post-analysis with UNLOC on the whole recorded dataset (up to 50,000 frames).

Cellular expression of β-tubulin and the nuclear pore protein Nup133 was imaged by dSTORM SMLM (Fig. 5). After chemical fixation, cells were incubated with primary antibodies before staining detection with fluorescently labeled secondary antibodies. Samples were imaged in freshly prepared dSTORM buffer, and laser power and camera integration time were adjusted to image β-tubulin in COS-7 cells and Nup133 in HeLa cells, respectively. QCM QC on given imaging conditions prior to acquisition can be based on just a few hundred frames, making it fast enough to avoid distortion in the recording of whole datasets due to lengthy adjustment procedures (e.g., due to photobleaching or dSTORM buffer deterioration) (Video S3). For example, the initial QCM analyses of β-tubulin imaging in COS-7 cells were carried out on just 2000 frames displaying informative and robust SNR and D_{frame} histograms (Fig. 5 *a*). The QCM analyses can also be made throughout data recording to allow the tracking over time of indicator mean values and the resulting assessment of their stability or inconsistency, for instance, in the event of focal plane loss. Finally, QCM and UNLOC analyses carried out on the same number of frames show that 35% and 49% of detected signals have an estimated accuracy greater than or equal to 20 nm for β-tubulin and Nup 133, respectively (Fig. 5 *b*).

Among other SMLM methods, DNA-PAINT, based on the transient association of a fluorescently labeled probe with a target molecule, has become particularly popular due to the ability to adjust experimental conditions to the expression level of the proteins of interest being visualized. The signal detection is mediated by pairing a docking oligonucleotide coupled to a target probe that recognizes a protein of interest coupled to an imager, i.e., a fluorescently labeled complementary oligonucleotide freely diffusing in the buffer (45). This method depends on the concentration of the imager that controls the density of transient docker/imager hybridization per frame, enabling a stochastic detection of the protein of interest by recording fluorescence signals.

For two-color DNA-PAINT experiments (Fig. 6), we used an automated workflow system to sequentially deliver the

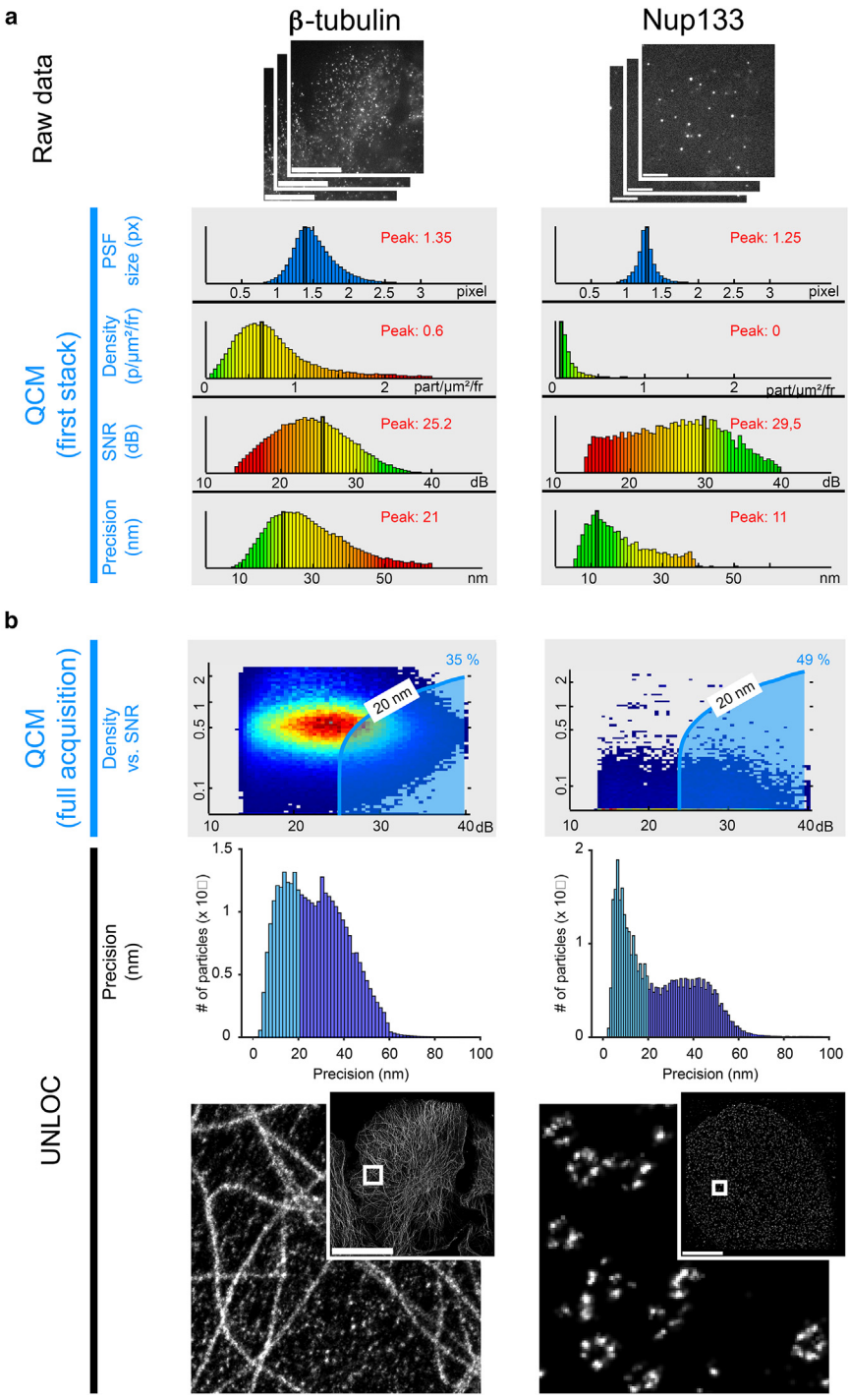

FIGURE 5 QCM-optimized dSTORM acquisitions. dSTORM imaging of β-tubulin and Nup133 labeling in COS-7 and HeLa cells, respectively. (*a*) QCM histograms and maps were computed from the first 2000 frames. (*b*) Postacquisition analysis of the complete set of recorded raw data. The density-SNR space diagrams displayed by QCM for β-tubulin and Nup133 reveal that 36% and 49% of detected particles have a localization accuracy (precision) better than 20 nm, respectively. UNLOC showing the integrated Gaussian reconstructed images for particles with localization accuracy better than 20 nm. Scale bars: 20 μm (inset: 5 μm on a side) and 5 μm (inset: 1.5 μm on a side) for β-tubulin and Nup133, respectively.

respective imagers into a channel slide to detect the mitochondrial 20 kDa outer membrane protein TOM20 and the major building block of microtubules α-tubulin in HeLa cells (see materials and methods). For acquisitions at appropriate D_{frame}, the imager concentrations were preadjusted using QCM over just 500 frames, i.e., an acquisition time of 18 s, as shown in Fig. 6 *b*, to define the conditions required for TOM20 protein imaging. QCM analyses were performed at three successive imager concentrations on the same sample preparation. The 1.5 nM concentration proved too high and significantly impaired localization accuracy. At 0.3 nM, the QCM provided significant intracellular variability in D_{frame} and SNR values, with poorly resolved areas as illustrated in the inset. At a 10-fold lower imager concentration, i.e., 30 pM, QCM provided adequate localization accuracy for TOM20 in any intracellular area.

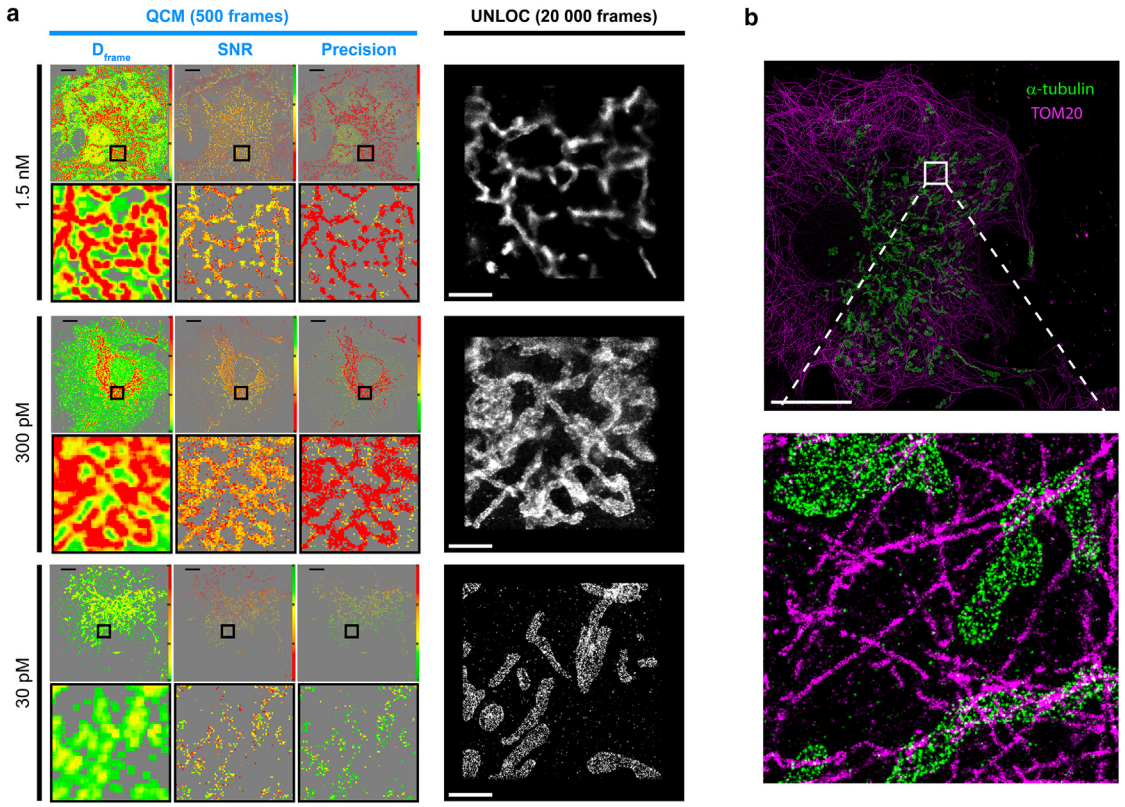

FIGURE 6 QCM-optimized acquisitions of two-color DNA-PAINT data. (*a*) Detection of TOM20 in HeLa cells by DNA-PAINT imaging on 500 frames. Real-time QCM analyses at different imager concentrations anticipates incorrect and inappropriate acquisitions based on poor D_{frame}, SNR, and localization accuracy (precision) indicator values at imager concentrations above 30 pM. Postacquisition analyses on the full stack of 20,000 frames validate the quality control observations, as shown by the shape of the mitochondrial network in the reconstructed images by UNLOC. Scale bars: 10 μm (in the insets: 1 μm). (*b*) Reconstructed images from postprocessed α-tubulin and TOM20 data with UNLOC. The concentrations of imagers for two-color DNA-PAINT acquisition with sequential fluid exchange were preadjusted with QCM. Scale bars: 20 μm (in the inset: 2 μm on a side).

The relevance of the QCM analyses obtained on a few hundred images is demonstrated by their comparison with the reconstructed images obtained using UNLOC on complete datasets. We thus detected the distribution of TOM20 and α-tubulin in HeLa cells. QCM has demonstrated sufficient efficiency to allow adjustment of experimental conditions in real time to ensure optimal DNA-PAINT-based multicolor sequential localization of multiple cellular components, such as TOM20 and α-tubulin, as illustrated by the integrated Gaussian reconstructed images from the postprocessed UNLOC analyses (Fig. 6 *b*). QCM thus appears as a key asset for unlocking the power of multicolor DNA-PAINT SMLM approaches (Video S4).

DISCUSSION

In line with FAIR principles (38), smart microscopes have emerged that incorporate tools, such as QCM, to enable quantitative data analysis and effective feedback for real-time readjustment of key parameters (46). The interactive capability of QCM encourages more adaptive experimentation and reduced number of trial-and-error cycles, which is especially important for such biological samples for which access is limited.

As compared to other currently available software solutions (30,32,33,35,47–49), QCM is a user-friendly software package, requiring no parameters other than those characterizing the optical system; nonexpert users can, therefore, easily operate it. Overall, QCM features an optimized software interface and display with easy-to-evaluate color-coded maps and histograms generated in real time. This instantaneous quantitative information enables parameter adjustment, the optimization of imaging conditions, and the dynamic exploration of subregions of interest in the sample. Assessing such QC of raw SMLM data at the earliest steps of acquisition enables acceptance or rejection decisions to be made on the basis of just a few hundred images and thus optimizes the amount of data to be acquired, stored, and analyzed for proper quantification of relevant observables.

The overall computation rate currently achievable by the UFUL module is primarily based on a one-Gaussian fitting hypothesis, i.e., for low D_{frame} values, ideally below 0.2 particles/μm^2/frame. We have accordingly integrated in QCM a calibration of the density evaluation to provide

more accurate D_{frame} estimations. In some circumstances, samples present a nonuniform distribution of the molecules (21,23). Consequently, it is advisable to perform postprocessing analyses of the recorded SMLM data with algorithms based on a multi-Gaussian fitting hypothesis. In this framework, we previously implemented UNLOC, a parameter-free algorithm approaching the CRB for particles at high D_{frame} and without any prior knowledge of their intensity (36).

We would like to underline that the QCM offline mode offers invaluable possibilities for use with postacquisition SMLM data. We further stress that this mode is perfectly suited to carrying out standardized studies with no a priori assumptions on reusable SMLM raw metadata or for reviewing publications including SMLM data. QCM is also of general interest for teaching basic SMLM concepts to a wide audience. Overall, QCM can be seamlessly integrated into the workflow of in-house or commercial systems and cloud-based data analysis frameworks.

At present, we have succeeded in analyzing 2048 × 2048 pixel images at a rate of over 100 fps, a rate fast enough to explore dynamic processes in living samples. While it may be possible to record data at a faster acquisition rate—for example, by focusing on a small ROI—we might face an intrinsic limitation of the SMLM technique due to the number of photons collected being, at some point, limiting. Alternatives such as the promising event-based vision sensor-based imaging method (50) for *in vivo* imaging are paving the way toward a very promising paradigm shift in cell biology by providing access to a new quantitative set of relevant observables.

ACKNOWLEDGMENTS

The authors thank Dr. Jérôme Touvier for his initial work on this project, Dr. Marc Allain (Institut Fresnel) for his deep reading of the UFUL part, Dr. Rémi Lasserre for general discussions, the Photonics facility of the Institut Fresnel and Emily Witty (AngloScribe) for language editing.. A CC-BY-NC 4.0 public copyright license has been applied by the authors to the present document and will be applied to all subsequent versions up to the author-accepted manuscript arising from this submission, in accordance with the grant's open access conditions. This work is supported by institutional funding from the French National Institute of Health and Medical Research (INSERM), Centre National de la Recherche Scientifique (CNRS), Centrale Marseille, and Aix-Marseille-Université (AMU) and program grants from the French National Research Agency (ANR-10-INBS-04, ANR-18-CE15-0021-02, and ANR-21-CE44-0026-02 to D.M.) and SATT Sud-Est (SATT N°191702 to D.M.). We acknowledge use of the PICsL-FBI imaging facility present within the Center d'Immunologie Marseille Luminy (ImagImm), a member of the national France-BioImaging infrastructure.

AUTHOR CONTRIBUTIONS

N.B., S.M., and D.M. conceived the project. N.B. and S.M. developed the algorithm. M.D. and R.F. performed the experiments to extensively test the software. D.M. supervised this work and prepared the original draft with the support of N.B. and S.M. All authors revised and edited the manuscript.

DECLARATION OF INTERESTS

R.F. is now an employee of the Carl Zeiss SAS-France company.

SUPPORTING MATERIAL

Supporting material can be found online at https://doi.org/10.1016/j.bpj.2025.02.018.

REFERENCES

1. Carpenter, A. E., B. A. Cimini, and K. W. Eliceiri. 2023. Smart microscopes of the future. *Nat. Methods.* 20:962–964. https://doi.org/10.1038/s41592-023-01912-0.
2. Strack, R. 2020. Smarter microscopes. *Nat. Methods.* 17:23. https://doi.org/10.1038/s41592-019-0708-0.
3. Royer, L. A., W. C. Lemon, …, P. J. Keller. 2016. Adaptive light-sheet microscopy for long-term, high-resolution imaging in living organisms. *Nat. Biotechnol.* 34:1267–1278. https://doi.org/10.1038/nbt.3708.
4. Mahecic, D., W. L. Stepp, …, S. Manley. 2022. Event-driven acquisition for content-enriched microscopy. *Nat. Methods.* 19:1262–1267. https://doi.org/10.1038/s41592-022-01589-x.
5. Hell, S. W., and J. Wichmann. 1994. Breaking the diffraction resolution limit by stimulated emission: stimulated-emission-depletion fluorescence microscopy. *Opt. Lett.* 19:780–782. https://doi.org/10.1364/ol.19.000780.
6. Betzig, E., G. H. Patterson, …, H. F. Hess. 2006. Imaging intracellular fluorescent proteins at nanometer resolution. *Science.* 313:1642–1645. https://doi.org/10.1126/science.1127344.
7. Rust, M. J., M. Bates, and X. Zhuang. 2006. Sub-diffraction-limit imaging by stochastic optical reconstruction microscopy (STORM). *Nat. Methods.* 3:793–795. https://doi.org/10.1038/nmeth929.
8. Vogelsang, J., R. Kasper, …, P. Tinnefeld. 2008. A reducing and oxidizing system minimizes photobleaching and blinking of fluorescent dyes. *Angew Chem. Int. Ed. Engl.* 47:5465–5469. https://doi.org/10.1002/anie.200801518.
9. Virant, D., I. Vojnovic, …, U. Endesfelder. 2023. Unraveling the kinetochore nanostructure in Schizosaccharomyces pombe using multi-color SMLM imaging. *J. Cell Biol.* 222:e202209096. https://doi.org/10.1083/jcb.202209096.
10. Sauer, M., and M. Heilemann. 2017. Single-Molecule Localization Microscopy in Eukaryotes. *Chem. Rev.* 117:7478–7509. https://doi.org/10.1021/acs.chemrev.6b00667.
11. Mund, M., and J. Ries. 2020. How good are my data? Reference standards in superresolution microscopy. *Mol. Biol. Cell.* 31:2093–2096. https://doi.org/10.1091/mbc.E19-04-0189.
12. Baumgart, F., A. M. Arnold, …, G. J. Schütz. 2016. Varying label density allows artifact-free analysis of membrane-protein nanoclusters. *Nat. Methods.* 13:661–664. https://doi.org/10.1038/nmeth.3897.
13. Schnell, U., F. Dijk, …, B. N. G. Giepmans. 2012. Immunolabeling artifacts and the need for live-cell imaging. *Nat. Methods.* 9:152–158. https://doi.org/10.1038/nmeth.1855.
14. Tanaka, K. A. K., K. G. N. Suzuki, …, A. Kusumi. 2010. Membrane molecules mobile even after chemical fixation. *Nat. Methods.* 7:865–866. https://doi.org/10.1038/nmeth.f.314.
15. Jimenez, A., K. Friedl, and C. Leterrier. 2020. About samples, giving examples: Optimized Single Molecule Localization Microscopy. *Methods.* 174:100–114. https://doi.org/10.1016/j.ymeth.2019.05.008.
16. Whelan, D. R., and T. D. M. Bell. 2015. Image artifacts in Single Molecule Localization Microscopy: why optimization of sample preparation protocols matters. *Sci. Rep.* 5:7924. https://doi.org/10.1038/srep07924.

17. Coelho, S., J. Baek, …, K. Gaus. 2020. Ultraprecise single-molecule localization microscopy enables *in situ* distance measurements in intact cells. *Sci. Adv.* 6:eaay8271. https://doi.org/10.1126/sciadv.aay8271.
18. Reinhardt, S. C. M., L. A. Masullo, …, R. Jungmann. 2023. Angstrom-resolution fluorescence microscopy. *Nature.* 617:711–716. https://doi.org/10.1038/s41586-023-05925-9.
19. Lelek, M., M. T. Gyparaki, …, C. Zimmer. 2021. Single-molecule localization microscopy. *Nat. Rev. Methods Primers.* 1:39. https://doi.org/10.1038/s43586-021-00038-x.
20. Štefko, M., B. Ottino, …, S. Manley. 2018. Autonomous illumination control for localization microscopy. *Opt. Express.* 26:30882–30900. https://doi.org/10.1364/OE.26.030882.
21. Martens, K. J. A., B. Turkowyd, and U. Endesfelder. 2021. Raw Data to Results: A Hands-On Introduction and Overview of Computational Analysis for Single-Molecule Localization Microscopy. *Front. Bioinform.* 1:817254. Technology and Code. https://doi.org/10.3389/fbinf.2021.817254.
22. Lee, A., K. Tsekouras, …, S. Pressé. 2017. Unraveling the Thousand Word Picture: An Introduction to Super-Resolution Data Analysis. *Chem. Rev.* 117:7276–7330. https://doi.org/10.1021/acs.chemrev.6b00729.
23. Khater, I. M., I. R. Nabi, and G. Hamarneh. 2020. A Review of Super-Resolution Single-Molecule Localization Microscopy Cluster Analysis and Quantification Methods. *Patterns (N Y).* 1:100038. https://doi.org/10.1016/j.patter.2020.100038.
24. Culley, S., D. Albrecht, …, R. Henriques. 2018. Quantitative mapping and minimization of super-resolution optical imaging artifacts. *Nat. Methods.* 15:263–266. https://doi.org/10.1038/nmeth.4605.
25. Marenda, M., E. Lazarova, …, D. Michieletto. 2021. Parameter-free molecular super-structures quantification in single-molecule localization microscopy. *J. Cell Biol.* 220:e202010003. https://doi.org/10.1083/jcb.202010003.
26. Sage, D., H. Kirshner, …, M. Unser. 2015. Quantitative evaluation of software packages for single-molecule localization microscopy. *Nat. Methods.* 12:717–724. https://doi.org/10.1038/nmeth.3442.
27. Sage, D., T. A. Pham, …, S. Holden. 2019. Super-resolution fight club: assessment of 2D and 3D single-molecule localization microscopy software. *Nat. Methods.* 16:387–395. https://doi.org/10.1038/s41592-019-0364-4.
28. Munro, I., E. García, …, P. M. W. French. 2019. Accelerating single molecule localization microscopy through parallel processing on a high-performance computing cluster. *J. Microsc.* 273:148–160. https://doi.org/10.1111/jmi.12772.
29. Diekmann, R., M. Kahnwald, …, J. Ries. 2020. Optimizing imaging speed and excitation intensity for single-molecule localization microscopy. *Nat. Methods.* 17:909–912. https://doi.org/10.1038/s41592-020-0918-5.
30. Li, L., B. Xin, …, Z.-L. Huang. 2019. Divide and conquer: real-time maximum likelihood fitting of multiple emitters for super-resolution localization microscopy. *Opt. Express.* 27:21029–21049. https://doi.org/10.1364/OE.27.021029.
31. Li, M., M. Shang, …, Z.-L. Huang. 2022. Real-time image resolution measurement for single molecule localization microscopy. *Opt. Express.* 30:28079–28090. https://doi.org/10.1364/OE.463996.
32. Gui, D., Y. Chen, …, Z. L. Huang. 2022. PCIe-based FPGA-GPU heterogeneous computation for real-time multi-emitter fitting in super-resolution localization microscopy. *Biomed. Opt. Express.* 13:3401–3415. https://doi.org/10.1364/BOE.459198.
33. Tang, Y., L. Dai, …, T. Gensch. 2015. SNSMIL, a real-time single molecule identification and localization algorithm for super-resolution fluorescence microscopy. *Sci. Rep.* 5:11073. https://doi.org/10.1038/srep11073.
34. Lin, J., K. Wang, and Z.-L. Huang. 2024. Real-time data processing in colorimetry camera-based single-molecule localization microscopy via CPU-GPU-FPGA heterogeneous computation. *Biomed. Opt. Express.* 15:5560–5573. https://doi.org/10.1364/BOE.534941.
35. Hauser, F., and J. Jacak. 2021. Real-time 3D single-molecule localization microscopy analysis using lookup tables. *Biomed. Opt. Express.* 12:4955–4968. https://doi.org/10.1364/BOE.424016.
36. Mailfert, S., J. Touvier, …, N. Bertaux. 2018. A Theoretical High-Density Nanoscopy Study Leads to the Design of UNLOC, a Parameter-free Algorithm. *Biophys. J.* 115:565–576. https://doi.org/10.1016/j.bpj.2018.06.024.
37. Serge, A., N. Bertaux, …, D. Marguet. 2008. Dynamic multiple-target tracing to probe spatiotemporal cartography of cell membranes. *Nat. Methods.* 5:687–694. https://doi.org/10.1038/nmeth.1233.
38. Wilkinson, M. D., M. Dumontier, …, B. Mons. 2016. The FAIR Guiding Principles for scientific data management and stewardship. *Sci. Data.* 3:160018. https://doi.org/10.1038/sdata.2016.18.
39. Papoulis, A., and S. U. Pillai. 2002. Probability, Random Variables, and Stochastic Processes. McGraw-Hill.
40. Huang, B., W. Wang, …, X. Zhuang. 2008. Three-dimensional super-resolution imaging by stochastic optical reconstruction microscopy. *Science.* 319:810–813. https://doi.org/10.1126/science.1153529.
41. Kay, S. M. 2009. Fundamentals of Statistical Processing, Volume 2: Detection Theory. Pearson Education.
42. Page, V., F. Goudail, and P. Refregier. 1999. Improved robustness of target location in nonhomogeneous backgrounds by use of the maximum-likelihood ratio test location algorithm. *Opt Lett.* 24:1383–1385. https://doi.org/10.1364/ol.24.001383.
43. Poor, H. V. 1994. An Introduction to Signal Detection and Estimation, 2nd ed. Springer-Verlag.
44. Raab, M., I. Jusuk, …, P. Tinnefeld. 2018. Using DNA origami nanorulers as traceable distance measurement standards and nanoscopic benchmark structures. *Sci. Rep.* 8:1780. https://doi.org/10.1038/s41598-018-19905-x.
45. Jungmann, R., C. Steinhauer, …, F. C. Simmel. 2010. Single-molecule kinetics and super-resolution microscopy by fluorescence imaging of transient binding on DNA origami. *Nano Lett.* 10:4756–4761. https://doi.org/10.1021/nl103427w.
46. Scherf, N., and J. Huisken. 2015. The smart and gentle microscope. *Nat. Biotechnol.* 33:815–818. https://doi.org/10.1038/nbt.3310.
47. Henriques, R., M. Lelek, …, M. M. Mhlanga. 2010. QuickPALM: 3D real-time photoactivation nanoscopy image processing in ImageJ. *Nat. Methods.* 7:339–340. https://doi.org/10.1038/nmeth0510-339.
48. Kechkar, A., D. Nair, …, J. B. Sibarita. 2013. Real-time analysis and visualization for single-molecule based super-resolution microscopy. *PLoS One.* 8:e62918. https://doi.org/10.1371/journal.pone.0062918.
49. Griffié, J., T. A. Pham, …, D. Sage. 2020. Virtual-SMLM, a virtual environment for real-time interactive SMLM acquisition. Preprint at bioRxiv. https://doi.org/10.1101/2020.03.05.967893.
50. Cabriel, C., T. Monfort, …, I. Izeddin. 2023. Event-based vision sensor for fast and dense single-molecule localization microscopy. *Nat. Photonics.* 17:1105–1113. https://doi.org/10.1038/s41566-023-01308-8.